Journal of Materials Chemistry C

ROYAL SOCIETY OF CHEMISTRY

PAPER

View Article Online
View Journal | View Issue

Cite this: J. Mater. Chem. C, 2022, 10, 9222

Triphenylene-ethylammonium tetrachlorometallate salts: multicolumnar mesophases, thermochromism and Langmuir films†‡

María Barcenilla, [a] María Jesús Baena, [a] Bertrand Donnio, *[b] Benoît Heinrich, [b] Lucía Gutiérrez, [c] Silverio Coco *[a] and Pablo Espinet *[a]

Received 18th March 2022,
Accepted 27th May 2022

DOI: 10.1039/d2tc01100j

rsc.li/materials-c

This study reports new mesomorphic benzylethylammonium salts containing a 2,3,6,7,10-pentakis(dodecyloxy)-11-(hexyloxy)triphenylene unit and Cl^- or $[MCl_4]^{2-}$ (M = Cu, Ni, Co, Mn) as counterions. They show a rich columnar polymesomorphism, characterized by polarized optical microscopy (POM), differential scanning calorimetry (DSC), and small- and wide-angle X-ray scattering (S/WAXS). All the compounds self-organize into multisegregated structures in the solid state and in the mesophases, with the alternation within large superlattices of triphenylene-containing columns and benzylammonium chloride or tetrachorometallate fragments. Interestingly, the nickel derivative displays a continuous and reversible thermochromic behavior in the range of 50–80 °C. Magnetic measurements and UV-Vis data at different temperatures, support changes in the coordination sphere of the Ni(II) atom from octahedral to tetrahedral. Furthermore, these systems form stable and homogeneous Langmuir films at the air–water interface. These films have been successfully transferred onto solid substrates giving rise to nanostructured LB films with a clearly defined bilayer structure in which each layer consists of molecular columns aligned along the surface.

Introduction

Building low-cost devices with flexible and easily processable components is a strongly desired objective in soft electronic technology. This requires new functional materials with predetermined physical properties. A representative case is that of functional columnar liquid crystals with specific optical, electric or magnetic properties that can be combined with the supramolecular organization and fluidity of the liquid crystalline mesophases.[1–8] Triphenylene-based mesogens are part of a widely studied subclass of columnar liquid crystals.[9,10] Their properties can be modulated through tailoring of the triphenylene core with a variety of functional groups,[11–15] including metal-organic complexes.[16–21] In this sense, we have reported mesomorphic metal-organic complexes containing triphenylene moieties,[22–24] where the luminescent properties of the mesophase[25] and the charge mobility along the columnar stacking[26,27] are modulated by the metal fragment.

Thermochromic materials are also promising functional materials for multiple applications, such as energy-saving windows,[28,29] temperature indicators,[30,31] display instruments[32] or security materials.[33] They can be designed for a variety of materials including liquid crystals,[34] polymers,[35] and metal-containing complexes.[36] In the liquid crystals field, the thermochromic behaviour produced by chiral mesophases is well known and widely used for the preparation of thermoindicators. Thermochromic liquid crystals based on non-chiral systems are relatively scarce and mainly correspond to columnar metallomesogens, in which the colour change is attributed to the variation of the interdisc distance with temperature, or to phase transitions in the case of calamitic systems.[37,38] In non-mesogenic metal complexes, this behaviour is usually due to a change in

[a] IU CINQUIMA/Química Inorgánica, Facultad de Ciencias, Universidad de Valladolid, 47071 Valladolid, Castilla y León, Spain. E-mail: silverio.coco@uva.es, espinet@qi.uva.es

[b] Institut de Physique et Chimie des Matériaux de Strasbourg (IPCMS), UMR 7504 (CNRS-Université de Strasbourg), F-67034 Strasbourg Cedex 2, France. E-mail: bertrand.donnio@ipcms.unistra.fr

[c] Dept. Química Analítica, Instituto de Nanociencia y Materiales de Aragón (INMA), CSIC-Universidad de Zaragoza and Ciber-BBN, Zaragoza 50018, Spain

† This work is dedicated to honor Professor Peter M Maitlis, who has passed away at the age of 89 when the revision of this paper was to be submitted. Maitlis was an outstanding and dedicated man of science and a human example for all those who had the privilege to work close with him. We owe him much more than the word "metallomesogens".

‡ Electronic supplementary information (ESI) available: Materials and methods, full details of synthetic methods, spectroscopic and analytical data for the new compounds, DSC thermograms and X-ray diffraction patterns not included in the text. See DOI: https://doi.org/10.1039/d2tc01100j

either the crystalline phase, the geometry of the metal centre, or the number of solvent molecules in the structure.[36]

Looking for thermochromic liquid crystals based on metal complexes that can induce metal-centred thermochromism without the need of chiral structures, we have chosen to study triphenylene-ethylammonium salts (TPh-NH_2Et^+) of potentially thermochromic Cu(II), Ni(II), Co(II) and Mn(II) tetrachlorometallates. For instance, it is known that $(NEt_2H_2)_2[NiCl_4]$ shows a reversible thermochromic behavior.[40] Furthermore, these designed molecular structures, inspired by other previous structurally reported materials,[23,26] made of a triphenylene unit connected to a benzylammonium salt *via* an alkyl spacer, were expected to lead to the formation of multicolumnar mesophases, as both immiscible species should phase separate and be confined in different regions in the mesophase. As an additional aspect of interest, these systems may form stable Langmuir films at the air/water interface, which could be transferred very efficiently to glass substrates to give Langmuir-Blodgett films with well-ordered bilayer structures.

Results and discussion

Synthesis and characterization

The unreported triphenylene derivative [TPh-NH_2Et]Cl (**3**) was prepared from the corresponding aldehyde as shown in Scheme 1. The ethylammonium tetrachlorometallate salts (**4–7**) were synthesized by direct reaction of **3** with the corresponding metal chloride MCl_2 (Scheme 1) and isolated as coloured solids in 88–98% yield. For synthetic and characterization details, see ESI.‡

The structures of conventional $(R_2NH_2)_2[MCl_4]$ complexes (M = Cu, Ni, Mn, Co, R = alkyl) reported in the literature can be taken as reasonable models to **4–7**. In the solid state, these structures consist of an alternation of anionic metal halide layers partitioned by arrays of cations. The inorganic regions of the copper,[39] nickel,[40] and manganese[41,42] compounds consist of distorted MCl_6 octahedra featuring MCl_4 layers of square planar metal centres sharing bridging chloro ligands, and two apical terminal Cl ligands on each metal centre.[43] At variance with those, reported tetrahedral $[CoCl_4]^{2-}$ groups were found in the cobaltate salts.[44]

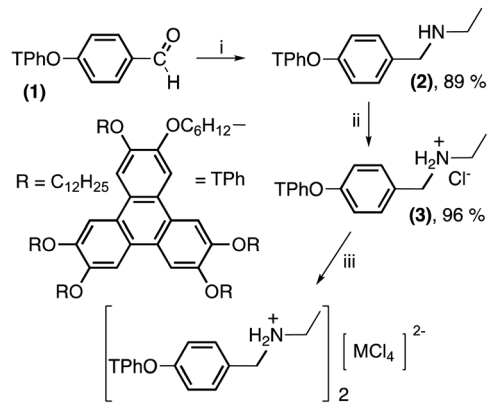

M = Cu (**4**, 95 %), Ni (**5**, 88 %), Co (**6**, 96 %), Mn (**7**, 98 %)

Scheme 1 Synthesis of the Cl^- and $[MCl_4]^{2-}$ salts of [TPhO-C_6H_4-CH_2-$NH_2Et]^+$ (**3–7**). i: (a) $EtNH_2$, THF; (b) $NaBH_4$, THF + EtOH. ii: HCl, CH_2Cl_2. iii: MCl_2, CH_2Cl_2/EtOH.

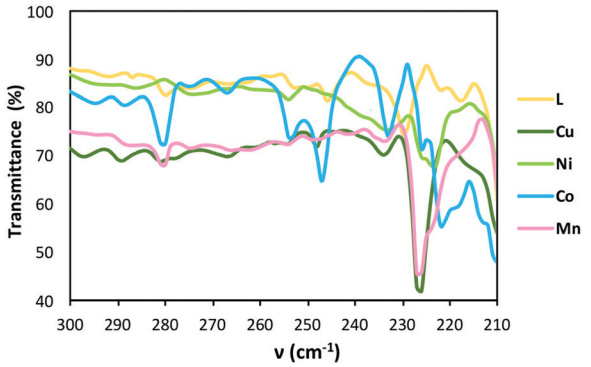

Fig. 1 Far-infrared spectra of TPh-NH_2Et^+ salts at 298 K (L = Cl^- salt; M = $[MCl_4]^{2-}$ salt).

Consistent with these literature data, the IR spectra of the Cu, Mn and Ni salts **4**, **5**, and **7** (Fig. 1) are typical of octahedral, polymeric materials containing bridging halo-ligands, with an absorption at *ca.* 226 cm^{-1}.[40] In contrast, the cobalt salt **6** displays a single absorption at 282 cm^{-1}, assigned to ν(Co–Cl) in a tetrahedral $[CoCl_4]^{2-}$ anion.[44]

The electronic spectra of the **4–7** TPh-NH_2Et^+ salts in the solid state (diffuse reflectance) at room temperature display a spectral pattern with absorption bands in the range 240–400 nm, corresponding to the 2,3,6,7,10,11-hexaalkoxytriphenylene group (Fig. 2).[45,46] The cobaltate salt shows, in addition, an intense absorption band at lower energy assigned to an $^4A_2 \rightarrow {}^4T_1(^4P)$ transition in the tetrahedral $[CoCl_4]^{2-}$ group.[47] In contrast, for the other tetrachlorometallate derivatives only broad low-intensity absorption bands in the range 400–480 nm are observed, in accordance with their octahedral or distorted-octahedral coordination geometries (Fig. 2).[48]

Thermal behaviour and self-organization properties

The mesomorphic properties of [TPh-NH_2Et]Cl (**3**) and the four tetrachlorometallate salts (**4–7**) have been studied by polarized

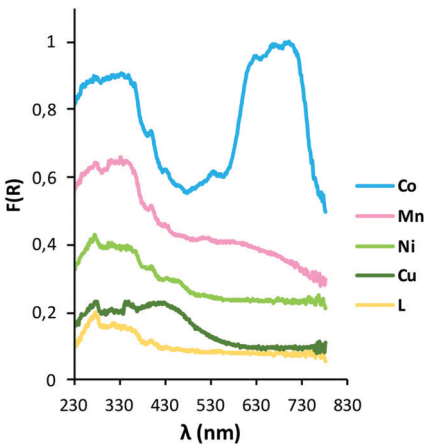

Fig. 2 UV-Vis spectra of the TPh-NH_2Et^+ salts in the solid state (diffuse reflectance) at 298 K (L = Cl^- salt; M = $[MCl_4]^{2-}$ salt).

optical microscopy (POM), differential scanning calorimetry (DSC), and small- and wide-angle X-ray scattering (S/WAXS). The optical, thermal and thermodynamic data are gathered in Table 1. Representative microphotographs are shown in Fig. 3. The mesophase assignment of Table 1 is based on the results of the S/WAXS studies. Additional data are provided in the ESI.‡

All the compounds show good stability up to temperatures above 200 °C (Fig. S12–S15, ESI‡), and display enantiotropic mesophases, as deduced from the observation of fluid and birefringent optical textures (Fig. 3 and Table 1). Either two (for **3**,**4**,**5**) or three (for **6**,**7**) mesophases are detected between the melting and the clearing point in the DSC cycles, both in the heating and in the cooling, confirming the polymesomorphism of these compounds (Fig. S7–S11 in the ESI‡). The textures observed by POM on cooling from the isotropic liquid, similar for all compounds, are *a priori* compatible with the occurrence of columnar mesophases.[26,34] However, their unambiguous exact identification from the textures observed is not possible.

A more precise identification of the liquid crystalline mesophases was achieved by S/WAXS. The patterns recorded for all compounds in their pristine state and at various temperatures (Fig. S16–S20, Table 2 and Table S1 in ESI‡) confirm that the complexes self-organize into multisegregated columnar structures, with the alternation within large superlattices of TPh-containing columns and benzylammonium chloride or tetrachorometallate salts (labelled as BzaS = Benzylamonium-Salt) embedded in an aliphatic continuum. The pristine states are characterized by the presence of one sharp small-angle peak, several unresolved diffused signals over the S/WAXS angular range, and a slightly structured broad signal in the wide-angle range, corresponding to incompletely molten aliphatic chains, an indication of partially crystallized solid state with still high

Table 1 Optical, thermal, and thermodynamic data for the TPh-NH_2Et^+ salts

Cpd	Transition[a]	T^b (°C)	ΔH^b (kJ mol^{-1})
(3)	Cr → M	40.8	42.6
	M → Col_{rec}	80.1	2.6
	Col_{rec} → I	95.7	3.2
(4)	Cr → M	43.4	102.4
	M → Col_{rec}	99.7	2.7
	Col_{rec} → I	116.1	2.8
(5)[c]	Cr → M	44.6	108.3
	M → Col_{rec}	99.7	2.7
	Col_{rec} → I	120.4	6.0
(6)	Cr → M	43.6	95.7
	M → Col_{rec}	103.7	3.2
	Col_{rec} → Col_{hex}/Col_{squ}	126.5	1.8
	Col_{hex}/Col_{squ} → I	139.9	1.8
(7)[c]	Cr → M	45.4	104.3
	M → Col_{rec}	110.6	2.3
	Col_{rec} → Col_{hex}/Col_{squ}	124.2	0.3
	Col_{hex}/Col_{squ} → I	140.1	2.6

[a] Cr, crystal phase; M: unknown mesophase with a large superlattice; Col_{rec}, rectangular columnar mesophase; Col_{hex}, hexagonal columnar mesophase; Col_{squ}, square columnar mesophase; I, isotropic liquid; mesophase assignment based on S/WAXS studies. [b] Data collected from the second heating DSC cycle. The transition temperatures are given as peak onsets. [c] Scanning rate: 5 °C min^{-1}.

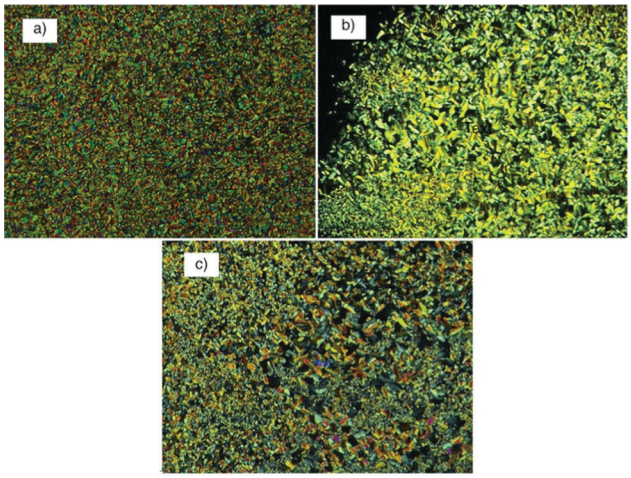

Fig. 3 Optical polarizing microscopy photographs (×100, crossed polarizers) on cooling from the isotropic phase of: (a) [TPh-NH_2Et]Cl (**3**) at 87 °C; (b) [TPh-NH_2Et]$_2$[$CuCl_4$] (**4**) at 109 °C; (c) [TPh-NH_2Et]$_2$[$NiCl_4$] (**5**) at 112 °C.

level of structural disorder. On further heating, the X-ray patterns are systematically transformed, in agreement with the induction of a more long-range supramolecular organization. Whilst still retaining the single sharp small-angle reflection, one could observe the development of the mid-angle broad scattering signal, labelled D, into a set of several not-well resolved but sharp reflections (Fig. 4 and Fig. S16–S20, ESI‡), and the splitting of the broad large-angle scattering into two different contributions, namely: (i) the strong one at *ca.* 4.5–4.6 Å, corresponding to the undifferentiated liquid-like lateral distances between aliphatic chains and spacers and benzylammonium-salt moieties, h_{ch} + h_{BzaS}, respectively; and (ii) the one at 3.5–3.6 Å, corresponding to the triphenylene units orthogonally stacked over short distances, h_π. At this stage, the nature and symmetry of this mesophase, M, could unfortunately not be unambiguously resolved, as too many indexation solutions were compatible with so few not-so-well resolved reflections. It could nevertheless correspond to a long-range, likely 3D, pre-organized structure of the mesophase forming at higher temperature.

The X-ray patterns were slightly modified on further heating, and all the sharp and strong reflections could be indexed according to a 2D rectangular symmetry (Table S1, ESI‡). In the wide-angle part, the split signals h_{ch} + h_{BzaS}/h_π of the preceding M phase was transformed into a single broad and extended wide-angle signal corresponding to the overall merging of all the various contributions (h = h_{ch} + h_{BzaS}+ h_π) (h_π, is hardly visible for compounds **3** and **7**, and has totally disappeared for the other compounds, in agreement with the reduction of the stacking distance to a few triphenylene units only). As just mentioned, in the small-angle range, they exhibit a set of several sharp small-angle reflections (hk) characterizing the two-dimensional arrangement of mesogenic columns separated in space by a molten aliphatic continuum. The presence of the underlying broad signal at intermediate angular range,

Table 2 Structural parameters

Cpds[a]	Phase[b]	2D lattice	V_{mol}[d]	$n_{BzaS/mol}$[e]	h_π [ξ]/h[f]	$Z_{col,BzaS}$[g]	
T (°C)	(Z)	parameters[c]	ρ	$n_{TPh/mol}$	Z_{mol}	$Z_{col,TPh}$	h_{TPh}[h]
3	Col_{rec}	a = 89.6(9);	2541	1	3.6 [2]/4.5	2	3.45
90	*c*2*mm*	b = 65.6(7);	0.94	1	8	8	
	(Z = 2)	γ = 90°;					
		A = 5890 Å^2;					
		a/b = 1.37					
4	Col_{rec}	a = 91.0(8);	5269	1	3.6 [2]/4.5	2	3.56
110	*c*2*mm*	b = 65.0(8);	0.95	2	4	8	
	(Z = 2)	γ = 90°;					
		A = 5927 Å^2;					
		a/b = 1.40					
5	Col_{rec}	a = 90.4(7);	5268	1	3.6 [2]/4.5	2	3.54
110	*c*2*mm*	b = 65.7(3);	0.95	2	4	8	
	(Z = 2)	γ = 90°;					
		A = 5947 Å^2;					
		a/b = 1.38					
6	Col_{rec}	a = 91.3(0);	5285	1	3.5 [2]/4.5	2	3.50
115	*c*2*mm*	b = 66.2(5);	0.94	2	4	8	
	(Z = 2)	γ = 90°;					
		A = 6049 Å^2;					
		a/b = 1.38					
6	Col_{hex}	$a = b$ = 57.6;	5352	1	—/4.3	1	3.73
135	*p*6*mm*		0.93	2	2	4	
	(Z = 1)	γ = 120°					
		A = 2871 Å^2					
	Col_{squ}	$a = b$ = 49.9;	5352	1	—/4.3	1	4.3
	*p*4*mm*	γ = 90°	0.93	2	2	4	
	(Z = 1)	A = 2490 Å^2					
7	Col_{rec}	a = 92.2(5);	5310	1	3.6 [2]/4.5	2	3.51
115	*c*2*mm*	b = 65.5(5);	0.94	2	4	8	
	(Z = 2)	γ = 90°;					
		A = 6047 Å^2;					
		a/b = 1.41					
7	Col_{hex}	$a = b$ = 58.0;	5360	1	—/4.3	1	3.68
135	*p*6*mm*	γ = 120°;	0.93	2	2	4	
	(Z = 1)	A = 2917 Å^2					
	Col_{squ}	$a = b$ = 50.3;	5360	1	—/4.3	1	4.2
	*p*4*mm*	γ = 90°	0.93	2	2	4	
	(Z = 1)	A = 2530 Å^2					

[a] T: temperature of the measurement. [b] Col_{rec}, $Col_{hex/squ}$: rectangular and hexagonal/square columnar mesophases and highest possible symmetry, Z: number of motifs (molecular aggregates) per lattice. [c] a, b, γ, $A = a \times b \times \sin\gamma$, a/b: lattice parameters, lattice area and lattice parameter ratio. [d] V_{mol} (Å^3), ρ (g cm^{-3}): calculated molecular volume and density. [e] $n_{BzaS/mol}$, $n_{TPh/mol}$: number of benzylammonium/anion units and number of TPh units per molecule (stoichiometry). [f] h_π, [ξ]: average π-stacking distance (Å) and associated correlation length from wide-angle scattering analysis (nm) calculated using the Scherrer equation with shape factor K = 0.9;[49] h: undifferentiated liquid-like contributions of the chains, BzaS and TPh moieties; Z_{mol}: number of molecules per lattice. [g] $Z_{col,BzaS} = Z$: number of benzylammonium/anion columns per lattice; $Z_{col,TPh} = Z_{mol} \times n_{TPh/mol}$: number of TPh columns per lattice. [h] $h_{TPh} = (V_{mol}/n_{TPh,mol})/(A/Z_{col,TPh})$: molecular slice thickness along TPh columns (Å).

D, was still detected, as for the mesophase M, which was associated to the development of some local-range superstructure.

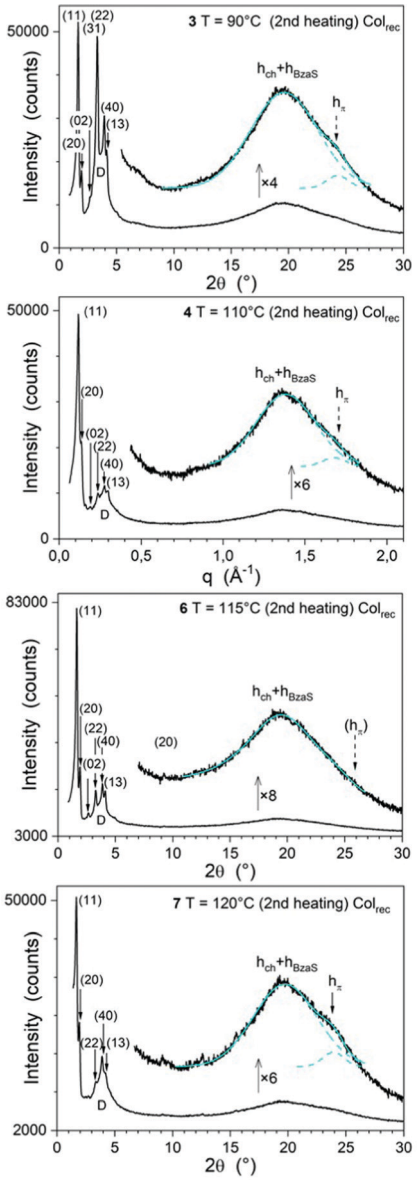

Fig. 4 Representative S/WAXS patterns of the compounds in the mesophase. *hk* indexation of the small-angle peaks; $h_{ch} + h_{BzaS}$, undifferentiated liquid-like lateral distances between aliphatic chains and spacers, and benzylammonium-salt moieties, respectively; h_π, triphenylene stacking over short distances; *D*, short-range correlated periodicity from the supramolecular assembly. For **6**, the signal cannot be deconvoluted since the stacking signal (h_π) is too weak, if not unexistent; its theoretical position (shown in brackets) is indicated by the dashed arrow.

Finally, as mentioned above, for the Co and Mn complexes an additional mesophase could be detected between the rectangular phase and the isotropic liquid. In the two cases, the only difference with the rectangular phase is the collapse of the mid-angle reflections into the single broad scattering signal, D, and the presence of only one sharp small-angle reflection. In the wide-angle, all signals from the chains, the BzaS and TPh units are overlapped into an undifferentiated single broad signal, *h*. On this basis, the mesophase could be assigned either as hexagonal (Col_{hex}) or as square (Col_{squ}) columnar mesophase.

In the isotropic liquid phase (Iso), the broad small-angle signal D was found to persist, which is due to some reminiscence of the nanosegregation still occurring at the local-range level between the TPh and the BzaS moieties. The single broad signal seen in the wide-angle range for the $Col_{hex/squ}$ phase is associated to undifferentiated liquid-like contributions of the chains, BzaS and TPh moieties.

The emergence of columnar mesophases with large superlattice structures, containing several columns per lattice (multicolumnar mesophases, see below), was thus confirmed for all compounds by the presence of several sharp, small-angle reflections, revealing lattices with large dimensions, along with the modulation of the reflections intensity distribution. These patterns also confirmed the efficient segregation between the various parts, namely, the triphenylene discs, the BzaS species (Cl^- or $[MCl_4^-]$ anions) and the chains. As expected, the mesomorphism induction for this kind of compounds is strongly driven by the tendency of the triphenylenes to stack into one-dimensional columns and to nanosegregate in space due to their peripheral alkyl chains. However, the BzaS fragments are also confined into separate zones, and their arrangement must respect the various geometrical constraints and the mesophase symmetry in each case. Therefore, these salts self-assemble in large superlattices of rectangular and hexagonal/square symmetries with the concerted entanglement of two subnetworks of several triphenylene-based columns and BzaS-based (metal-based) columns, respectively, each types being separated by the infinite continuum of molten alkyl chains.

As previously developed,[23,26] more intimate details about the respective organization of the two subsets of columns within the superlattices can be revealed from the ratio between the molecular volume (V_{mol}) and the lattice area (A, with $Z = 2$, for the rectangular symmetry, and $Z = 1$ for hexagonal/square symmetry), scaled by the total number of ligands or complexes per lattice, Z_{mol} (Table 2). This let us to deduce the number of TPh- and BzaS-based columns per lattice ($Z_{col,TPh} = Z_{mol} \times n_{TPh/mol}$, $Z_{col,BzaS} = Z$, respectively) by repeating trial-error tests and considering the most logical solution in agreement with the symmetry elements of the planar group, *i.e.* rectangular and hexagonal/square planar groups (Table 2). This calculation also provides a value for h_{TPh}, the molecular slice thickness along the TPh-based columns ($h_{TPh} = (V_{mol}/n_{TPh,mol})/(A/Z_{col,TPh})$), which lies close to the value of h_π, consistent with a nearly orthogonal stacking of the triphenylene discs in the columns.

For the rectangular phases, a value of 8 (for the precursor **3**) and 4 (for the complexes **4–7**) is deduced for Z_{mol}, respectively, which gives columnar rectangular superlattices containing 8 TPh- and 2 BzaS-based columns. A plausible supramolecular arrangement of the columns in the rectangular mesophase (Fig. 5) would consist of a stack of ammonium/metal fragments located at the nodes of the rectangular lattice (corners and centre, $Z_{col,BzaS} = 2$), intertwined by a network of 8 discoidal columns ($Z_{col,TPh}$), thus respecting the triphenylene-metal fragment stoichiometry, both separated by the aliphatic continuum, in complete agreement with the centred symmetry and

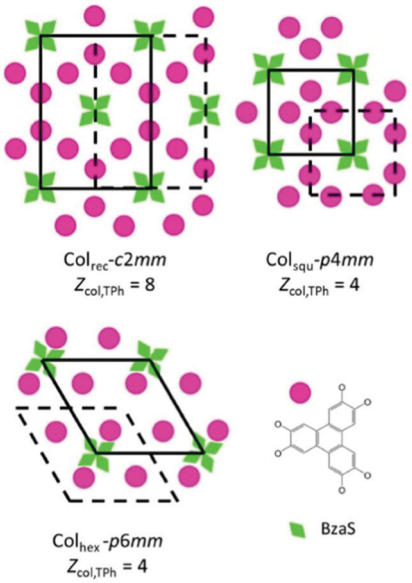

Fig. 5 Illustration of the proposed 2D packing for the Col_{rec} mesophase (*c2mm* symmetry), and for the Col_{squ} mesophase (*p4mm* symmetry), and for the Col_{hex} mesophase (*p6mm* symmetry). The pink disks correspond to TP-based columns, and the green petals to BzaS-based aggregates; the aliphatic chains, occupying the white areas, are not shown for clarity.

dimensions of the rectangular lattice, and the modulated distribution of the intensities of the higher order reflections.

As for the $Col_{hex/squ}$ phase of compounds **6** and **7**, these calculations give 2 complexes, whatever the symmetry considered, that indicates a self-assembly made of 4 TPh- and 1 BzaS-based columns (Table 2). From the S/WAXS patterns, it was not possible to discriminate between a columnar mesophase with hexagonal or square symmetry (only the fundamental reflection is seen), so both mesophases are equiprobable. Thus, a possibility for arranging the columns in the mesophase (Fig. 5) would consist of a stack of metal fragments located at the corners of the hexagonal/square lattice ($Z_{col,BzaS} = 1$), intertwined by a network of 4 discoidal columns ($Z_{col,TPh}$) within the lattice, also respecting the triphenylene-metal fragment stoichiometry, both types of columns being separated by the aliphatic continuum. The only difference, and this would be more in the favour to the square lattice, is the estimation of h_{TPh}, which gives a value of *ca.* 4.2–4.3 Å close to h (4.3 Å, Table 2), considering the square symmetry, whereas this calculation gives a value of *ca.* 3.7 Å for the hexagonal case.

Thermochromic behaviour

The nickel complex **5** is green at room temperature and switches to a bluish colour upon heating at about 60 °C (Fig. 6). The compound shows reversible thermochromic behaviour and, upon cooling to room temperature, it returns gradually to its original green colour.

In order to understand this colour change, the electronic spectra of a drop-cast film of **5** were recorded at different temperatures (Fig. 7).

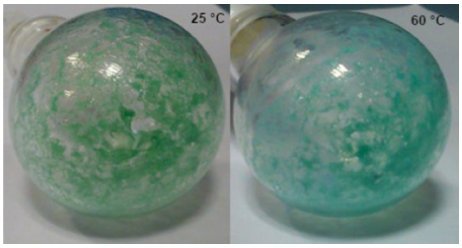

Fig. 6 Photographs of thermochromic complex [TPh-$NH_2Et]_2[NiCl_4]$ (**5**) at different temperatures.

As discussed in the synthesis and characterization section, before heating the electronic spectrum of **5** is dominated by absorption bands in the range 240–400 nm, corresponding to the 2,3,6,7,10,11-hexaalkoxytriphenylene group, which practically overlap the weak absorption band ($^3A_{2g}^{(F)} \rightarrow {}^3T_{1g}^{(P)}$ transition) corresponding to octahedrally coordinated nickel. When the sample is heated above 45 °C, a doublet absorption band appears, with maxima at 658 nm and 711 nm, which is typical of the blue tetrahedral $[NiC1_4]^{2-}$ complex anion ($^3T_1^{(F)} \rightarrow {}^3T_1^{(P)}$ transition).[40,48] Therefore, the thermochromic phase transition of the complex is assigned to the coordination change of Ni(II) from octahedral or distorted-octahedral to tetrahedral, as reported for related non-mesogenic complexes in the solid state.[48,50] According to the plot of absorbance *vs.* temperature (Fig. 8), the transition occurs between 50 and 80 °C. Thus, the thermochromic transition starts and develops along the melting process.

Magnetization measurements for the nickel compound at different temperatures were performed to assess the changes in magnetic properties associated to the thermochromic transformation. The resulting field dependent magnetization curves are shown in Fig. 9.

All the magnetization curves (Fig. 9) show an overall similar pattern, in which two different magnetic contributions are observed. Interestingly, when looking into detail, the field dependent magnetization curves at temperatures below the thermochromic transformation (3 and 27 °C) are different from those recorded at higher temperatures (77 and 100 °C), in agreement with the phase transition occurring between 50 and 80 °C.

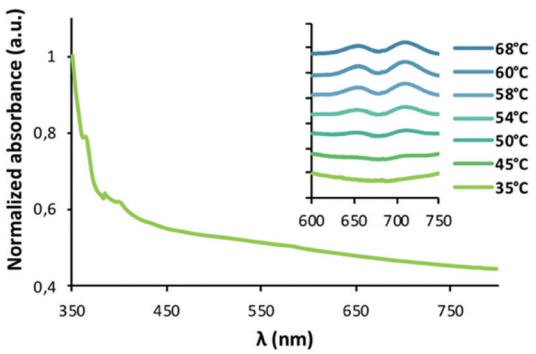

Fig. 7 Electronic spectrum of [TPh-$NH_2Et]_2[NiCl_4]$ (**5**) at 35 °C. Inset: Spectral changes produced upon varying the temperature.

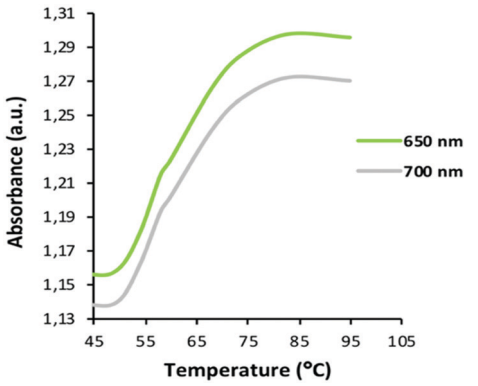

Fig. 8 Absorbance change at λ = 650 nm and λ = 700 nm as a function of temperature.

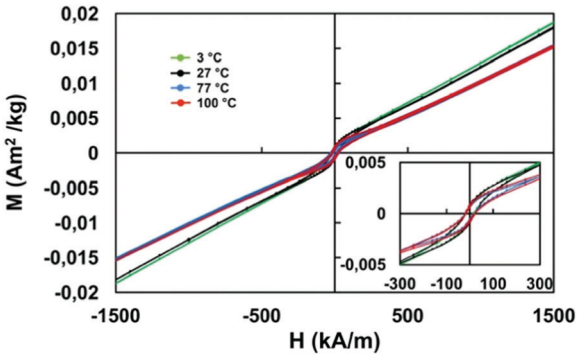

Fig. 9 Field dependent magnetization curve of the nickel compound (**5**) at different temperatures.

In all cases, in the low-field regime observed in the inset of Fig. 9, a hysteresis loop with non-negligible coercivity was recorded, indicating ferro- or ferrimagnetic interaction between the Ni(II) atoms. In addition to this magnetic contribution, a clear paramagnetic behaviour is observed at higher fields, revealed by the increase of the magnetization as the magnetic field increased, without any sign of saturation. These results indicated the co-existence of two types of environments of the Ni atoms within the material structure. This fact is in accordance with the X-ray data discussed above: (i) the partially crystalline nature of the solid phase and its high level of structural disorder; and (ii) the persistence in the mesophases of some local-range superstructure detected in the solid state.

Consequently, the ferro- or ferrimagnetic contribution can be assigned to the crystal structure of this type of compound, where distorted $Ni^{II}Cl_6$ octahedra are sharing bridging chloro ligands. However, the species contributing to the paramagnetic behaviour would be different depending on the temperature. At temperatures above thermotropic transition, the formation of tetrahedral tetrachloronickelate anions explains the presence of a paramagnetic signal. However, at lower temperatures, where this anion was not spectroscopically observed, the paramagnetic contribution should be associated with the

non-crystalline solid fraction, in which long-range ordering will not occur as in the crystalline fraction.

Langmuir films

Considering the amphiphilic nature of the mesomorphic TPh-NH_2Et^+ salts, we decided to study their ability to form 2D nanostructures at the air–water interface (Langmuir films). Compounds [TPh-NH_2Et]Cl (**3**) and [TPh-$NH_2Et]_2[NiCl_4]$ (**5**) were chosen as representative salts for this study. Both compounds form monolayer films under compression. Fig. 10 shows the surface pressure *vs.* mean molecular area (SP-A) obtained at 20 ± 1 °C, as well as the variation of the reciprocal of the compressibility ($1/\beta$).[51,52]

Both monolayer films undergo a phase transition between two liquid condensed (LC) phases, denoted by a minimum in $1/\beta$ which coincides with the slight inflection observed in the isotherm at 20–30 mN m^{-1}. The collapse is reached at high surface pressures (≈50 mN m^{-1}), revealing a good anchoring of the ionic heads to the subphase. In addition, the plateau that appears just after the collapse denotes the resistance of the monolayer respect to the transformation into a 3D phase.[53] In good agreement with its double content in TPh moieties, the formula unit of **5** occupies twice the area of that of **3**. However, the molecular area per triphenylene group is larger for **3** than for **5** despite the bigger volume of the $[NiCl_4]^{2-}$ anion. This is most likely due to the increase in the ionic charge in $[NiCl_4]^{2-}$ with respect to Cl^- which enhances the anion-cation attractions, increasing the film cohesion.

The films start to be formed with molecular areas per triphenylene of 127 ± 5 $Å^2$ (A_{onset}) and reach extrapolated to zero mean molecular areas (A_e) of 117 ± 4 $Å^2$ in the first step of the isotherm. These molecular areas together with the $1/\beta$ values indicate that the floating films of **3** and **5** are in a liquid condensed phase LC1 where the TPh moieties lay edge-on respect to the subphase.[54–56] On further compression, the LC1 phase evolves to another condensed but less rigid phase LC2, where the extrapolated areas are equal or slightly smaller than those in LC1 (see Fig. 10).

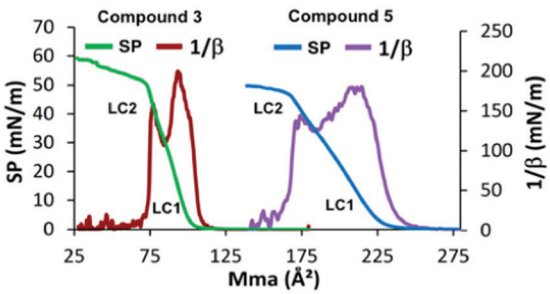

	A_{onset} (Å²/molec)	LC1 Phase A_e (Å²/molec)	LC2 Phase A_e (Å²/molec)	Collapse (mN/m)
3	132	121	119	49
5	244	227	227	47

Fig. 10 SP-A isotherms and $1/\beta - A$ plot for compounds **3** and **5**. Table: Molecular occupied areas at different phases and collapse pressure of the Langmuir films. LC = liquid condensed phase.

This behaviour is unlike that reported for the TPh-imidazolium or pyridinium salts,[55] where the monolayer firstly shows a liquid expanded (LE) phase, with the triphenylenes lying flat on the subphase, and then reaches a more rigid phase, but not LC, with the triphenylenes stacked edge-on. This different behaviour may be related with the fact that the longer chain length and the smaller size of the cationic heads in our compounds enhance the magnitude of the attractive interactions over the disaggregation power of the water.

Monitoring of the compression process by Brewster's angle microscopy (BAM) (Fig. S21 and S22 in ESI‡) shows that before compression, **3** and **5** exhibit irregular patches of condensed monolayers, in accordance with the high tendency of triphenylene groups to self-assembling through π–π intermolecular interactions. Thus, the compression process should start with aggregates whose structure most likely consists of columns of cations sandwiching a central region of anions.

As the pressure increases ($1 < \pi < 20$ mN m^{-1}), the approximation of the aggregates leads to the formation of a condensed monolayer (LC1) where the molecular arrangement is, as previously discussed, edge-on type with the triphenylene groups arranged in columns parallel to the subphase (Scheme 2). At higher pressures ($20 < \pi < 50$ mN m^{-1}), the compaction of the monolayer and the consequent increase of the repulsion between ions produce the phase transition from LC1 to LC2. BAM images of both phases show that the monolayer is constituted by different domains, which should be due to different domain orientations.[53] No differences could be appreciated at the phase transition but an increase in brightness, which is usually related to a denser packing as well as to an increase in the monolayer thickness. These observations along with the fact that the extrapolated areas in both phases do not display significant differences, suggest that LC1 and LC2

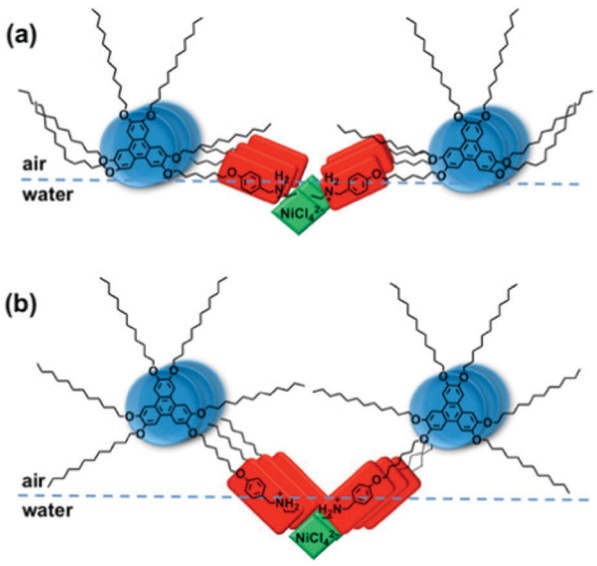

Scheme 2 Proposed columnar arrangement at the air–water interface corresponding to LC1 phase (a) and LC2 phase (b) adapted for compound **5**.

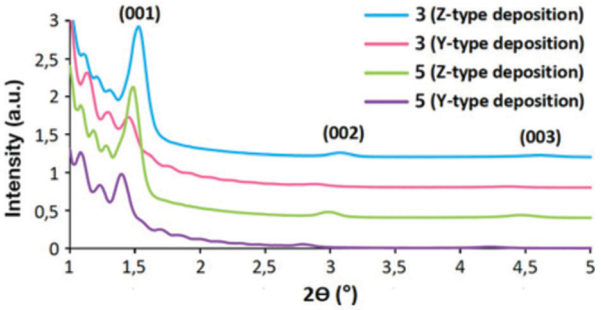

Fig. 11 Low-angle X-ray diffractograms for the LB films of **3** and **5**.

mainly differ in the molecular orientation of the TPh group with respect to the aqueous subphase. We propose that the TPh fragments rotate and only the ionic groups are anchored to the subphase in LC2, leading to columnar molecular arrangements as depicted in Scheme 2b.

Finally, formation of 3D structures (bright vertical lines) was not observed until overtaking the pressure of collapse, thus corroborating the above-mentioned resistance of the monolayer to that transformation.

Langmuir-Blodgett films

Langmuir films of **3** and **5** were transferred to glass substrates at two different pressures corresponding to LC2 (SP = 35 mN m^{-1}) and LC1 (SP = 15 mN m^{-1}) phases to build up Langmuir Blodgett (LB) films.

Good Y- and Z-type depositions were achieved, with transfer rates near to the unity, using hydrophobic and hydrophilic glasses respectively. To the best of our knowledge, there are no examples reported of Z-type LB films from discotic amphiphiles.[51,52,56–59]

The transversal structure of Z and Y-type multilayer LB films was studied by means of low-angle X-ray diffraction. The diffractograms corresponding to both type of LB films built at a constant compression of 35 mN m^{-1} are depicted in Fig. 11. All of them show three diffraction peaks corresponding to (00*l*) planes, as well as several sets of Kiessig fringes. This means that the LB films have a periodic layered structure with a small rugosity.[60] At 15 mN m^{-1}, similar bilayered structures have been obtained, but with smaller layer thickness (diffractograms in ESI‡), confirming that the thickness of the monolayer increases on passing from LC1 to LC2 phase, as above suggested. Table 3 collects the experimental planar distances and the mean layer thickness for each film.

Table 3 Low-angle XRD data for the LB films of **3** and **5**. All values in Å

		3	5
Y-Type deposition at LC2[a]	$d(00l)$[c]	61.2	63.5
	Layer thickness[d]	32.9	34.3
Z-Type deposition at LC2[b]	$d(00l)$	57.6	59.1
	Layer thickness	53.5	53.5
Z-Type deposition at LC1[b]	$d(00l)$	53.1	54.4
	Layer thickness	45.3	45.9

[a] Substrate = hydrophobized glass. [b] Substrate = hydrophilic glass. [c] Planar distances $d(00l)$ have been calculated by averaging the corresponding values of each diffraction peak. [d] The film thickness, t, was calculated from the periodicity of the Kiessig fringes substituting the slope a of the graph $sen\theta_n/n$ in the formula $t = \lambda/2a$.[60] The mean single layer thickness was calculated from the rate t/number of transferred monolayers.

It is worth noting that, independent of the deposition type, all the diffractograms display a similar pattern, which is consistent with analogous bilayer structures. A bilayer structure upon Y-deposition is the expected result. However, upon Z-deposition, the formation of a bilayer should require a reorganization of the deposited monolayer, as has been reported for LB films of fatty acids[61–63] or phospholipids.[64] Thus, it is plausible that the upstroke-transferred monolayer undergoes overturning during the subsequent immersion, acquiring a more stable bilayered structure with a new hydrophilic surface prone to adhere the following monolayer at upstroke.

Conclusions

This study shows the marked tendency of these triphenylene-benzylethylammonium derivatives to self-organize into multi-segregated structures. Structural studies support the nanosegregation of triphenylene columns and benzylammonium chloride or tetrachorometallate salt moieties, leading to multicolumnar systems, both in the solid state and in the mesophases. The thermal, optical and magnetic properties of these materials are easily modulated by the nature of the anion. The introduction of the tetrachloronickelate group leads to the combination of mesomorphism and thermochromism in the system. This compound shows visually a reversible thermochromic behaviour, light-green at room temperature and blue at 70 °C, which was studied with spectroscopical and magnetization measurements. The thermochromism in this compound implies a coordination change of the nickel(II) centre, from octahedral to tetrahedral, which is not simple. The magnetization measurements at different temperatures reveal the co-existence, in the conditions of the measurements, of two types of contributions of the Ni(II) atoms in the material, one corresponding to ferro- or ferrimagnetic interactions together with a paramagnetic behaviour that changes above thermotropic transition. In addition, these compounds self-assemble into nanostructured LB films with a well-defined bilayered structure where each layer is constituted by the alignment of molecular columns along the surface.

These results are interesting for future tailoring of metal-organic liquid crystals combining thermochromic and magnetic response.

Author contributions

The authors have contributed equally to the paper.

Conflicts of interest

There are no conflicts to declare.

Acknowledgements

This work was sponsored by the Ministerio de Ciencia e Innovación (Project PID2020-118547GB-I00) and the Junta de Castilla y León (Project VA224P20). M. B. thanks the Junta de Castilla y León for a PhD grant. BD and BH thank CNRS and the University of Strasbourg for support.

References

1 B. R. Kaafarani, *Chem. Mater.*, 2011, 378.
2 W. Pisula, M. Zorn, J. C. Chang, K. Müllen and R. Zentel, *Macromol. Rapid Commun.*, 2009, **30**, 1179.
3 T. Kato, T. Yasuda and Y. Kamikawa, *Chem. Commun.*, 2009, 729.
4 S. Sergeyev, W. Pisula and Y. H. Geerts, *Chem. Soc. Rev.*, 2007, **36**, 1902.
5 S. Laschat, A. Baro, N. Steinke, F. Giesselmann, C. Hägele, G. Scalia, R. Judele, E. Kapatsina, S. Sauer, A. Schreivogel and M. Tosoni, *Angew. Chem., Int. Ed.*, 2007, **46**, 4832.
6 A. W. Hains, Z. Liang, M. A. Woodhouse and B. A. Gregg, *Chem. Rev.*, 2010, **110**, 6689.
7 M. Oukachmih, P. Destruel, L. Seguy, G. Ablart, P. Jolinat, S. Archambeau, M. Mabiala, S. Fouet and H. Bock, *Sol. Energy Mater. Sol. Cells*, 2005, **85**, 535.
8 L. Schmidt-Mende, A. Fechtenkotter, K. Müllen, E. Moons, R. Friend and J. MacKenzie, *Science*, 2001, **293**, 1119.
9 T. Wohrle, I. Wurzbach, J. Kirres, A. Kostidou, N. Kapernaum, J. Litterscheidt, J. C. Haenle, P. Staffeld, A. Baro, F. Giesselmann and S. Laschat, *Chem. Rev.*, 2016, **116**, 1139.
10 S. K. Pal, S. Setia, B. S. Avinash and S. Kumar, *Liq. Cryst.*, 2013, **40**, 1769.
11 N. Boden, R. J. Bushby and A. N. Cammidge, *Liq. Cryst.*, 1995, **18**, 673.
12 N. Boden, R. J. Bushby, A. N. Cammidge and G. Headdock, *J. Mater. Chem.*, 1995, **5**, 2275.
13 S. Kumar, M. Manickam, V. S. K. Balagurusamy and H. Schonherr, *Liq. Cryst.*, 1999, **26**, 1455.
14 R. J. Bushby, N. Boden, C. A. Kilner, O. R. Lozman, Z. Lu, Q. Liu and M. A. Thornton-Pett, *J. Mater. Chem.*, 2003, **13**, 470.
15 N. Boden, R. J. Bushby, Z. B. Lu and A. N. Cammidge, *Liq. Cryst.*, 1999, **26**, 495.
16 S. Kumar and S. K. Varshney, *Liq. Cryst.*, 2001, **28**, 161.
17 J. L. Schulte, S. Laschat, R. Schulte-Ladbeck, V. von Arnim, A. Schneider and H. Finkelmann, *J. Organomet. Chem.*, 1998, **552**, 171.
18 A. N. Cammidge and H. Gopee, *Chem. Commun.*, 2002, 966.
19 B. Mohr, G. Wegner and K. Ohta, *Chem. Commun.*, 1995, 995.
20 F. Yang, X. Bai, H. Guo and C. Li, *Tetrahedron Lett.*, 2013, **54**, 409.
21 J. Shi, Y. Wang, M. Xiao, P. Zhong, Y. Liu, H. Tan, M. Zhu and W. Zhu, *Tetrahedron*, 2015, **71**, 463.
22 E. Tritto, R. Chico, G. Sanz-Enguita, C. L. Folcia, J. Ortega, S. Coco and P. Espinet, *Inorg. Chem.*, 2014, **53**, 3449.
23 A. B. Miguel-Coello, M. Bardají, S. Coco, B. Donnio, B. Heinrich and P. Espinet, *Inorg. Chem.*, 2018, **57**, 4359–4369.
24 R. Chico, C. Domínguez, B. Donnio, B. Heinrich, S. Coco and P. Espinet, *Cryst. Growth Des.*, 2016, **16**, 6984.
25 E. Tritto, R. Chico, J. Ortega, C. L. Folcia, J. Etxebarria, S. Coco and P. Espinet, *J. Mater. Chem. C*, 2015, **3**, 9385.
26 R. Chico, E. de Domingo, C. Domínguez, B. Donnio, B. Heinrich, R. Termine, A. Golemme, S. Coco and P. Espinet, *Chem. Mater.*, 2017, **29**, 7587.
27 E. de Domingo, C. L. Folcia, J. Ortega, J. Etxebarria, R. Termine, A. Golemme, S. Coco and P. Espinet, *Inorg. Chem.*, 2020, **59**, 10482.
28 H. Y. Lee, Y. Cai, S. Velioglu, C. Mu, C. J. Chang, Y. L. Chen, Y. Song, J. W. Chew and X. M. Hu, *Chem. Mater.*, 2017, **29**, 6947.
29 T. G. La, X. Li, A. Kumar, Y. Fu, S. Yang and H. J. Chung, *ACS Appl. Mater. Interfaces*, 2017, **9**, 33100.
30 S. Kumar, A. Qadir, F. Maury and N. Bahlawane, *ACS Appl. Mater. Interfaces*, 2017, **9**, 21447.
31 P. Liu, D. Zhou, Y. Wei, K. Jiang, J. Wang, L. Zhang, Q. Li and S. Fan, *ACS Nano*, 2015, **9**, 3753.
32 B. Ebru, M. Maxim, H. Borre, G. Anatoliy and W. John, *Jpn. J. Appl. Phys.*, 2006, **45**, 4146.
33 W. Zhang, X. Ji, C. Zeng, K. Chen, Y. Yin and C. Wang, *J. Mater. Chem. C*, 2017, **5**, 8169.
34 I. Sage, *Liq. Cryst.*, 2011, **38**, 1551.
35 A. Seeboth, D. Lötzsch, R. Ruhmann and O. Muehling, *Chem. Rev.*, 2014, **114**, 3037.
36 J. H. Day, *Chem. Rev.*, 1968, **86**, 649.
37 In *Metallomesogens*, ed. J. L. Serrano, VCH, Weinheim, 1996.
38 B. Donnio, D. Guillon, D. W. Bruce and R. Deschenaux, Metallomesogens, in *Comprehensive Organometallic Chemistry III: From Fundamentals to Applications*, ed. R. H. Crabtree and D. M. P. Mingos, Elsevier, Oxford, UK, 2006, vol. 12, ch. 12.05, p. 195.
39 J. P. Steadman and R. D. Willett, *Inorg. Chim. Acta*, 1970, **41**, 367.
40 J. R. Ferraro and A. T. Sherren, *Inorg. Chem.*, 1978, **17**, 2498.
41 R. D. Willett and E. F. Reidel, *Chem. Phys.*, 1975, **8**, 112.
42 L. Septiany, D. Tulip, M. Chislov, J. Baas and G. R. Blake, *Inorg. Chem.*, 2021, **60**, 15151.
43 G. Park, I.-H. Oh, J. M. S. Park, S.-H. Park, C. S. Hong and K.-S. Lee, *Phys. B*, 2018, **551**, 89.
44 A. Abkari, I. Chaabane and K. Guidara, *Phys. E*, 2017, **86**, 210.
45 D. Markovitsi, A. Germain, P. Millié, P. Lécuyer, L. K. Gallos, P. Argyrakis, H. Bengs and H. Ringsdorf, *J. Phys. Chem.*, 1995, **99**, 1005.
46 S. Marguet, D. Markovitsi, P. Millié, H. Sigal and S. Kumar, *J. Phys. Chem. B*, 1998, **102**, 4697.
47 H. Q. Yea, D. W. Lia, Q. Y. Maia, X. X. Chena, Q. Y. Chena, Y. Chena, J. R. Zhoua and C. L. Nia, *Synthesis and Reactivity in Inorganic, Metal-Organic, and Nano-Metal Chemistry*, 2014, **44**, 1368.
48 S. A. Kahani and F. Abdevali, *RSC Adv.*, 2016, **6**, 5116.

49 At small angles, the background depends on the angle and we therefore fitted this background around the peak, then subtract this fit before analyzing the peak itself. Even if the background is not a problem at large angles, we still considered it to calculate the correlation distances.
50 D. R. Bloomquist and R. D. Willett, *Coord. Chem. Rev.*, 1982, **47**, 125.
51 K. Iimura and T. Kato. Langmuir – Blodgett (LB) films, in *Organized Organic Ultrathin Films. Fundamentals and applications*, ed. K. Ariga, Wiley-WCH, 2013, ch. 3, p. 43.
52 J. T. Davies and E. K. Rideal, *Interfacial Phenomena*, Academic Press, New York, 1993.
53 A. Angelova, D. Vollhardt and R. Ionov, *J. Phys. Chem.*, 1996, **100**, 10710.
54 V. V. Tsukruk, H. Bengs and H. Ringsdorf, *Langmuir*, 1996, **12**, 754.
55 A. Nayak, K. A. Suresh, S. K. Pal and S. Kumar, *J. Phys. Chem. B*, 2007, **111**, 11157.
56 N. C. Maliszewskyj, P. A. Heiney, J. Y. Josefowicz, T. Plesnivy, H. Ringsdorf and P. Schumacher, *Langmuir*, 1995, **11**, 1666.
57 O. Karthaus, H. Ringsdorf, V. V. Tsukruk and J. H. Wendorff, *Langmuir*, 1992, **8**, 2279.
58 J. Y. Josefowicz, N. C. Maliszewskyj, S. H. J. Idziak, P. A. Heiney, J. P. McCauley, Jr. and A. B. Smith III, *Science*, 1993, **260**, 323.
59 A. Angelova and R. Ionov, *Langmuir*, 1996, **12**, 5643.
60 P. Tippmann-Krayer, H. Moehwald and Y. M. L'vov, *Langmuir*, 1991, **7**, 2298.
61 A. Momose, Y. Hirai, I. Waki, S. Imazeki, Y. Tomioka, K. Hayakawa and M. Naito, *Thin Solid Films*, 1989, **178**, 519.
62 J. D. K. Schwartz, R. Viswanathan and J. A. N. Zasadzinski, *Phys. Chem.*, 1992, **96**, 10444.
63 R. W. Corkery, *Langmuir*, 1997, **13**, 3591.
64 S. R. Rincón, A. Gonzalez-Orive, J. M. de la Fuente and P. Cea, *Langmuir*, 2017, **33**, 7538.